Asociación Argentina
de Mecánica Computacional

Mecánica Computacional Vol XXIX, págs. 3169-3184 (artículo completo)
Eduardo Dvorkin, Marcela Goldschmit, Mario Storti (Eds.)
Buenos Aires, Argentina, 15-18 Noviembre 2010

HOURGLASS CONTROL FOR THE STABILIZED FINITE ELEMENT SOLUTION OF COUPLED INCOMPRESSIBLE VISCOUS FLOWS AND HEAT TRANSFER

André L. Rossa[a], **José J. Camata**[b] **and Alvaro L. G. A. Coutinho**[b]

[a]*Engineering Simulation and Scientific Software, Florianópolis, SC, Brazil, arossa@esss.com.br, http://www.esss.com.br*

[b]*Federal University of Rio de Janeiro, NACAD, COPPE, Department of Civil Engineering, Rio de Janeiro, Brazil,{camata,alvaro}@nacad,ufrj.br, http://www.nacad.ufrj.br*

Keywords: stabilized formulation, incompressible flow, finite element method, reduced integration, adaptive mesh refinement.

Abstract.

This work presents an implementation of a stabilized finite element formulation for incompressible viscous flow coupled with the advective-diffusive temperature transport equation through the Boussinesq approximation approach. For solving of the incompressible Navier-Stokes equations we use the Streamline Upwind Petrov-Galerkin/Pressure Stabilized Petrov-Galerkin (SUPG/PSPG) formulation and for the advective transport equation the SUPG formulation is employed. A comparison of the computational performance between full Gaussian and reduced (centre of the element) integrations for the isoparametric 8-node hexahedron element is presented. A h-stabilization for both advective and viscous/diffusive terms is used to control the spurious *hourglass* modes introduced by under integrating the element. The implementation has been performed using the libMesh Finite Element Method (FEM) library (http://libmesh.sourceforge.net) which provides support for adaptive mesh refinement and coarsening (AMR/C) and parallel computations. A verification is made using the Kim-Moin problem and the computational performance is evaluated solving a natural convection problem in a parallel machine.

1 INTRODUCTION

The spatial integration on the domain of quadrilaterals and hexahedral elements in the finite element method is usually performed by Gaussian quadrature. When two- and three-linear interpolation functions are used, 2×2 integrations points, in two dimensions, and $2 \times 2 \times 2$ in three-dimensional problems are commonly employed.

Many computer codes that use explicit time integrations schemes adopt a lower quadrature order, which are less than that required for the exact spatial integration of the polynomials. Besides the large economy of computing time, especially in nonlinear problems, studies suggest that the convergence rate obtained with one-point quadrature is consistent with that obtained using the full integration (Belytschko et al., 1984) of the terms arising from the weak formulation which is the basis of the finite element method.

The main difficulty presented by one-point quadrature is the instability arising from oscillations in the solution. These oscillations result from the fact that the under-integrated gradient operator has no control over the spurious *hourglass* modes. Currently the pattern of oscillations is well known and is found in a wide range of physical problems (Mallet et al., 1992).

Many procedures have been developed to control the *hourglass* modes for the advective-diffusive terms in transport problems. Christon (1998) uses the so called h-stabilization performed through the outer product of the *hourglass* vectors of the elements to deduce the operator stabilizer which is added to the diffusive terms of the Navier-Stokes equations for solving incompressible viscous flow. In Mallet et al. (1992) is presented a correction to the *hourglass* modes for multidimensional advective-diffusive systems deduced from the Hu-Washizu variational formulation. This technique was applied to solve two- and three-dimensional Euler and Navier-Stokes equations for compressible flows using the Galerkin least-squares variational formulation with discontinuity capturing operator. Dias and Coutinho (1997) also derives from a Hu-Washizu variational formulation a technique to control the spurious oscillations to solve the two-dimensional scalar steady-state advective-diffusive equation using the SUPG formulation. Dias and Coutinho (2004) used a reduced integration technique together with a stabilized finite element method (FEM) formulation in the determination of the pressure and concentrations fields in a porous media.

Following the work of Mallet et al. (1992), this paper applies *hourglass* correction operators to under-integrated trilinear hexahedra for the finite element solution of coupled viscous flow and heat transfer problems. The SUPG/PSPG finite element formulation (Tezduyar, 1992) is used to discretize in space the incompressible Navier-Stokes equations, while the temperature transport equation is discretized by the SUPG finite element formulation.

In order to keep the focus on the issues related to the numerical problem, we use the libMesh framework. libMesh is a C++ library for parallel adaptive mesh refinement/coarsening numerical multiphysics simulations based on the finite element method (Kirk et al., 2006).

The remainder of this paper is organized as follows. In the next section we present the governing equations for coupled viscous flow and temperature transport, the corresponding finite element formulation and the *houglass* control operators. In Section 3 we present a verification problem, the Kim-Moin flow, and the solution of a three-dimensional natural convection to evaluate the parallel computing performance. The paper ends with a summary of our main conclusions.

2 MATHEMATICAL FORMULATION

2.1 Governing Equations

We consider the following velocity-pressure formulation of the Navier-Stokes equations governing incompressible viscous flow

$$\begin{aligned} \rho\left(\frac{\partial \mathbf{u}}{\partial t}+\mathbf{u}\cdot\nabla\mathbf{u}\right)-\mathbf{f}-\nabla\cdot\boldsymbol{\sigma}=0 \quad &\text{on } \Omega\times[0,t]\,, \\ \nabla\cdot\mathbf{u}=0 \quad &\text{on } \Omega\times[0,t]\,, \end{aligned} \tag{1}$$

where ρ is the density. $\mathbf{u}$ is the velocity and $\mathbf{f}$ is the body force carrying the gravity acceleration effect. $\boldsymbol{\sigma}$ is the stress tensor given as

$$\boldsymbol{\sigma}(p,\mathbf{u})=-p\mathbf{I}+\mathbf{T}, \tag{2}$$

where p is the hydrostatic pressure, $\mathbf{I}$ is the identity tensor and $\mathbf{T}$ is the deviatoric stress tensor

$$\mathbf{T}=2\mu\boldsymbol{\epsilon}(\mathbf{u})\,. \tag{3}$$

In equation (3) μ is the dynamic viscosity and $\boldsymbol{\epsilon}(\mathbf{u})$ is the strain rate tensor defined as

$$\boldsymbol{\epsilon}(\mathbf{u})=\frac{1}{2}\left(\nabla\mathbf{u}+(\nabla\mathbf{u})^T\right). \tag{4}$$

The essential and natural boundary conditions associated with equation (1) can be imposed at different portions of the boundary Γ and are represented by

$$\begin{aligned} \mathbf{u}=\mathbf{g} \quad &\text{on } \Gamma_{\mathbf{g}}, \\ \mathbf{n}\cdot\boldsymbol{\sigma}=\mathbf{h} \quad &\text{on } \Gamma_h. \end{aligned} \tag{5}$$

The advective-diffusive temperature transport is described by the following partial differential equation

$$\rho c_p\left(\frac{\partial T}{\partial t}+\mathbf{u}\cdot\nabla T)\right)-\nabla\cdot(\mathbf{k}\nabla T)=0, \tag{6}$$

where T is the temperature, c_p is the specific heat and $\mathbf{k}$ the conductivity tensor. The essential and natural boundary conditions are

$$\begin{aligned} T=T_g \quad &\text{on } \Gamma_{\mathbf{g}}, \\ -\mathbf{n}\cdot(\mathbf{k}\nabla T)=\mathbf{q} \quad &\text{on } \Gamma_{\mathbf{q}}. \end{aligned} \tag{7}$$

The coupling between the Navier-Stokes and temperature transport equations is done by the flotation forces due the small variations in the fluid density. These variations are calculated by Boussinesq approach which introduced in the body force vector results in the following equation

$$\mathbf{f}=\mathbf{g}\rho(T)\,, \tag{8}$$

where $\mathbf{g}$ is the gravity acceleration vector and $\rho(T)$ is the dependence of the fluid density on temperature variation given as

$$\rho(T)=\rho_\infty(1-\beta(T-T_\infty))\,. \tag{9}$$

In equation (9) ρ_∞ is the reference density of the fluid calculated at the reference temperature T_∞ and the parameter β is the thermal expansion coefficient.

2.2 Stabilized Formulation

We consider a suitably defined finite-dimensional trial solution and test function spaces for velocity and pressure, S_p^h, $V_{\mathbf{u}}^h$ and S_p^h and $V_p^h = S_p^h$. The stabilized finite element formulation of the momentum and continuity equations (1) for incompressible fluid flows can be written as: find $\mathbf{u} \in S_{\mathbf{u}}^h$ and $p \in S_p^h$ such as $\forall \mathbf{w}^h \in S_p^h$ and $\forall q^h \in S_p^h$

$$\begin{aligned}
&\int_\Omega \mathbf{w}^h \cdot \left[\rho\left(\frac{\partial \mathbf{u}^h}{\partial t} + \mathbf{u}^h \cdot \nabla \mathbf{u}^h\right) - \mathbf{f}\right] d\Omega + \int_\Omega \epsilon\left(\mathbf{w}^h\right) : \boldsymbol{\sigma}\left(p^h, \mathbf{u}^h\right) d\Omega - \int_\Gamma \mathbf{w}^h \cdot \mathbf{h} d\Gamma + \\
&\int_\Omega q^h \nabla \cdot \mathbf{u}^h d\Omega + \\
&\sum_{e=1}^{n_{el}} \int_{\Omega^e} \left(\tau_{SUPG} \mathbf{u}^h \cdot \nabla \mathbf{w}^h\right) \cdot \left[\rho\left(\frac{\partial \mathbf{u}^h}{\partial t} + \mathbf{u}^h \cdot \nabla \mathbf{u}^h\right) - \nabla \cdot \boldsymbol{\sigma}\left(p^h, \mathbf{u}^h\right) - \mathbf{f}\right] d\Omega^e + \\
&\sum_{e=1}^{n_{el}} \int_{\Omega^e} \left(\frac{1}{\rho} \tau_{PSPG} \nabla q^h\right) \cdot \left[\rho\left(\frac{\partial \mathbf{u}^h}{\partial t} + \mathbf{u}^h \cdot \nabla \mathbf{u}^h\right) - \nabla \cdot \boldsymbol{\sigma}\left(p^h, \mathbf{u}^h\right) - \mathbf{f}\right] d\Omega^e = 0.
\end{aligned} \tag{10}$$

The first four integrals in (10) arise from the classical Galerkin formulation. The summations over the elements are the SUPG and the PSPG stabilizations. The parameters for both stabilizations adopted in this work were obtained from Tezduyar (1992) and are defined as follows

$$\tau_{SUPG} = \tau_{PSPG} = \tau = \left[\left(\frac{2\left|\mathbf{u}^h\right|^2}{h^e}\right) + 9\left(\frac{4\nu}{h^{e2}}\right)\right]^{-1/2}, \tag{11}$$

where ν is the kinematic viscosity and h^e is an element length measure based in its volume V^e as shown bellow

$$h^e = \sqrt[3]{\frac{6V^e}{\pi}}. \tag{12}$$

For the temperature test functions we adopt the same assumptions. So S_T^h and V_T^h are the trial and test function spaces for the temperature equation and the stabilized finite formulation for the advective-diffusive transport can be written: find $T^h \in S_T^h$ such that $\forall \mathbf{w}^h \in V_T^h$

$$\begin{aligned}
&\int_\Omega \mathbf{w}^h \cdot \rho c_p \left(\frac{\partial T^h}{\partial t} + \mathbf{u}^h \cdot \nabla T^h\right) d\Omega + \int_\Omega \nabla \mathbf{w}^h \cdot \mathbf{k} \cdot \nabla T^h d\Omega - \int_\Gamma \mathbf{w}^h \cdot \mathbf{q} d\Gamma + \\
&\sum_{e=1}^{n_{el}} \int_{\Omega^e} \left(\tau_{SUPG} \mathbf{u}^h \cdot \nabla \mathbf{w}^h\right) \cdot \left[\rho c_p \left(\frac{\partial T^h}{\partial t} + \mathbf{u}^h \cdot \nabla T^h\right) - \nabla \cdot \mathbf{k} \cdot \nabla T\right] d\Omega^e = 0.
\end{aligned} \tag{13}$$

The first three integrals are from the Galerkin formulation over (13) and the summation over the elements is the SUPG stabilization. The SUPG parameter is calculated in a similar fashion to the defined above and is given as

$$\tau_{SUPG} = \tau_t = \left[\left(\frac{2\left|\mathbf{u}^h\right|^2}{h^e}\right) + 9\left(\frac{4k}{h^{e2}}\right)\right]^{-1/2}, \tag{14}$$

where k is the thermal diffusivity.

2.3 *Hourglass* Control Operators

The matrices integrated at the center of the element resulting from terms of equations (10) and (13) where the discretized gradient of the shape functions appears are rank deficient. It may cause spurious oscillations on the solution. Thus it is necessary to use a methodology able to suppress the under integration negative effects. Given three-linear interpolation functions N^k, ($k = [1, 8]$) we define $\mathbf{b}_i$ as the discrete gradient operator calculated at the centre of the element in the directions $i = x, y, z$,

$$\mathbf{b}_i = \left[N^1_{,i}, N^2_{,i}, N^3_{,i}, N^4_{,i}, N^5_{,i}, N^6_{,i}, N^7_{,i}, N^8_{,i}\right]^T . \tag{15}$$

Following Mallet et al. (1992), the interpolation of any scalar v over a typical element may be written as

$$v\left(x, y, z\right) = \left(\mathbf{C}^T + b^T_x x + b^T_y y + b^T_z z + \gamma^T_\alpha h_\alpha\right) \mathbf{v}^e, \tag{16}$$

where $\mathbf{v}^e$ are its local (element) nodes values array. The subscript $\alpha = 1, 2, 3, 4$ represents the four *hourglass* modes in the three-dimensional space. The vectors $\mathbf{C}$ and γ_α are calculated as

$$\mathbf{C} = \frac{1}{8}\left[\mathbf{t} - \mathbf{t}^T\mathbf{x}^e\mathbf{b}_x - \mathbf{t}^T\mathbf{y}^e\mathbf{b}_y - \mathbf{t}^T\mathbf{z}^e\mathbf{b}_z\right], \tag{17}$$

$$\gamma_\alpha = \frac{1}{V^e}\left[\mathbf{H}_\alpha - \mathbf{H}^T_\alpha\mathbf{x}^e\mathbf{b}_x - \mathbf{H}^T_\alpha\mathbf{y}^e\mathbf{b}_y - \mathbf{H}^T_\alpha\mathbf{z}^e\mathbf{b}_z\right], \tag{18}$$

where V^e is the element volume. In (16) the h_α functions are defined as follows

$$\begin{aligned} h_1 &= \frac{V^e}{8}\xi\eta, \\ h_2 &= \frac{V^e}{8}\eta\zeta, \\ h_3 &= \frac{V^e}{8}\xi\zeta, \\ h_4 &= \frac{V^e}{8}\xi\eta\zeta. \end{aligned} \tag{19}$$

where ξ, η, ζ are local natural coordinates at the reference space.

The vectors $\mathbf{t}$ and $\mathbf{H}_\alpha$ mean the rigid body motion and the hourglass modes and are given bellow

$$\mathbf{t} = [1, 1, 1, 1, 1, 1, 1, 1]^T , \tag{20}$$

$$\begin{aligned} \mathbf{H}_1 &= [1, -1, 1, -1, 1, -1, 1, -1]^T , \\ \mathbf{H}_2 &= [1, 1, -1, -1, -1, -1, 1, 1]^T , \\ \mathbf{H}_3 &= [1, -1, -1, 1, -1, 1, 1, -1]^T , \\ \mathbf{H}_4 &= [-1, 1, -1, 1, 1, -1, 1, -1]^T . \end{aligned} \tag{21}$$

The hourglass stabilizations for the advective and diffusive terms are derived introducing this new interpolation function on the Hu-Washizu variational formulation over the stabilized formulations (10) and (13). A discussion on the details of this procedure is beyond the scope of this work. One can found a complete deduction with further details in the work referenced above as well in Dias and Coutinho (1997) and Dias and Coutinho (2004).

Generally, the diffusive stabilization terms may be written as

$$d^{hg} = \epsilon_d \mathbf{D}_{ij} \mathcal{H}_{ii}^{\alpha\beta} \gamma_\alpha \gamma_\beta^T, \tag{22}$$

where $\mathbf{D}_{ij}$ is a generic diffusive tensor $(i, j = x, y, z)$ and

$$\mathcal{H}_{ii}^{\alpha\beta} = \int_{\Omega^e} h_{\alpha,i} h_{\beta,i}, \tag{23}$$

where $h_{\alpha,i}$ means the partial derivative with respect to a physical coordinate.

The advective stabilizations terms may be written in a general way as

$$a^{hg} = \epsilon_a \mathcal{X}_{ij}^{\alpha} \mathbf{b}_j \bar{u}_i^h \gamma_\alpha^T, \tag{24}$$

$$\mathcal{X}_{ij}^{\alpha\beta} = \int_{\Omega^e} x_j h_{\alpha,i}, \tag{25}$$

$\bar{u}_i^h$ is the average of each velocity component i at the centroid of the element and x_j are the global system coordinates.

Finally the (pressure) gradient stabilization term is given by

$$\mathbf{p}^{hg} = \epsilon_p \mathcal{X}_{ij}^{\alpha} \mathbf{b}_j \delta_{ij} \gamma_\alpha^T, \tag{26}$$

where δ_{ij} is the Kroenecker delta.

The stabilization (26) can be view as an advective stabilization term of a constant homogeneous advective field which its components are taken equal to 1.

In (22), (22) and (26) the non-dimensional hourglass stabilization parameters ϵ_k, $(k = d, a, p)$ may assume values in the range $[0, 1]$. The choice of its value is not trivial for elements with non-parallel faces. In this work, by default it was set as unity. See Gresho et al. (1984) and Belytschko et al. (2000) for further informations.

Remark 1. One should note that (22), (24) and (26) are 8×8 matrices and a sum must be done over the greek and latin indexes, i. e.,

$$d^{hg}(m, n) = \sum_\alpha \sum_\beta \sum_i \sum_j \mathbf{D}_{ij} \mathcal{H}_{ii}^{\alpha\beta} \gamma_\alpha(m) \gamma_\beta(n). \tag{27}$$

Equation (26) has one component for each cartesian direction, thus

$$p_j^{hg}(m, n) = \sum_\alpha \sum_\beta \sum_i \mathcal{X}_{ij}^{\alpha\beta} \mathbf{b}_j(m) \gamma_\alpha(n). \tag{28}$$

Remark 2. The $\mathcal{H}_{ij}^{\alpha}$ and $\mathcal{X}_{ij}^{\alpha}$ are performed using a symbolic algebra software while $\mathbf{b}_i$ and the diffusive tensors are evaluated at the element centroid (i.e. 1×1).

2.4 Discretized Systems

Adopting the implicit backward Euler scheme for the time discretization together with a fixed point linearization, the final discrete system of (10) and (13) (see Rossa et al. (2009)) plus the *hourglass* stabilization terms results in

$$\begin{aligned}&\left(\mathbf{M}^c+\mathbf{M}^s_\tau\right)\mathbf{u}^{n+1,\nu+1}+\Delta t\left(\mathbf{N}^s\left(\mathbf{u}^{n+1,\nu}\right)+\mathbf{N}^s_\tau\left(\mathbf{u}^{n+1,\nu}\right)+\mathbf{K}^s\right)\mathbf{u}^{n+1,\nu+1}-\\&\Delta t\left(\mathbf{G}^s-\mathbf{G}_\tau\right)\mathbf{p}^{n+1,\nu+1}=\Delta t\left(\mathbf{f}\left(\mathbf{T}^n\right)+\mathbf{f}_\tau\left(\mathbf{T}^n\right)\right)+\left(\mathbf{M}^c+\mathbf{M}^s_\tau\right)\mathbf{u}^n,\end{aligned} \tag{29}$$

$$\begin{aligned}&\Delta t\mathbf{G}^{sT}\mathbf{u}^{n+1,\nu+1}+\mathbf{M}^s_\xi\mathbf{u}^{n+1,\nu+1}+\Delta t\left(\mathbf{N}_\xi\left(\mathbf{u}^{n+1,\nu}\right)\mathbf{u}^{n+1,\nu+1}+\mathbf{G}^s_\xi\mathbf{p}^{n+1,\nu}\right)=\\&\Delta t\mathbf{f}_\xi\left(\mathbf{T}^n\right)+\mathbf{M}^s_\xi\mathbf{u}^n,\end{aligned} \tag{30}$$

$$\begin{aligned}&\left(\mathbf{M}^c+\mathbf{M}^s_\tau\right)\mathbf{T}^{n+1,\nu+1}+\Delta t\left(\mathbf{N}^s\left(\mathbf{u}^{n+1}\right)+\mathbf{N}^s_\tau\left(\mathbf{u}^{\nu}\right)+\mathbf{K}^s\right)\mathbf{T}^{n+1,\nu+1}=\\&\left(\mathbf{M}^c+\mathbf{M}^s_\tau\right)\mathbf{T}^n.\end{aligned} \tag{31}$$

In (29), (30) and (31) $\mathbf{u}$, $\mathbf{p}$ and $\mathbf{T}$ are the nodal vectors of the correspondent unknowns $\mathbf{u}^h$, $\mathbf{p}^h$ and $\mathbf{T}^h$. The super indexes $n+1$ and n mean the current and previous time steps while $\nu+1$ and ν are respectively the current and previous linear iterations.

For the matrices where the advective operator appears, i.e., Galerkin advection, SUPG mass and advection, and PSPG advection, the velocity components are evaluated at each integration point. Thus they are taken as the average at the center of the elements for the one point Gaussian integration.

The Galerkin mass matrix was analytically integrated considering the Jacobian determinant calculated at the centre of the element and is given bellow

$$\mathbf{M}^c=\frac{V^e}{64}\begin{bmatrix} a & b & c & b & b & c & d & c\\ & a & b & c & c & b & c & d\\ & & a & b & d & c & b & c\\ & & & a & c & d & c & b\\ & & & & a & b & c & b\\ & & \text{sym.} & & & a & b & c\\ & & & & & & a & b\\ & & & & & & & a\end{bmatrix} \tag{32}$$

where

$$\begin{aligned}a&=2.370370370370370\cdots,\\ b&=1.185185185185185\cdots,\\ c&=0.592592592592592\cdots,\\ d&=0.296296296296296\cdots.\end{aligned} \tag{33}$$

This mass matrix is a good approximation for the Galerkin mass matrix when the hexahedron presents a favorable aspect ratio.

$\mathbf{N}\left(\mathbf{u}\right)$ is the non-linear advection matrix, $\mathbf{G}$ and $\mathbf{G}^T$ are the gradient and its transpose (divergent) matrices. $\mathbf{f}$ is the body force vector. The matrices and vectors with the subscripts τ

and ξ mean the SUPG and PSPG terms. Moreover the matrices with the superscript s are those which the *hourglass* stabilizations terms were added, i.e.

$$\begin{aligned}
\mathbf{N}^s &= \mathbf{N} + \mathbf{N}^{hg} \\
\mathbf{K}^s &= \mathbf{K} + \mathbf{K}^{hg} \\
\mathbf{G}^s &= \mathbf{G} + \mathbf{G}^{hg} \\
\mathbf{M}^s_\tau &= \mathbf{M}_\tau + \mathbf{M}^{hg}_\tau \\
\mathbf{N}^s_\tau &= \mathbf{N}_\tau + \mathbf{N}^{hg}_\tau \\
\mathbf{M}^s_\xi &= \mathbf{M}_\xi + \mathbf{M}^{hg}_\xi \\
\mathbf{G}^s_\xi &= \mathbf{G}_\xi + \mathbf{G}^{hg}_\xi
\end{aligned} \tag{34}$$

where the superscript hg means the stabilization matrices which are summarized in the Table 1.

System	Matrix	Stabilization
Navier-Stokes	Advective Galerkin	$\mathcal{X}^{\alpha}_{ij}\mathbf{b}_j\bar{u}^h_i\gamma^T_\alpha$
	Viscous Galerkin	$\mu\mathbf{I}\mathcal{H}^{\alpha\beta}_{ii}\gamma_\alpha\gamma^T_\beta$
	Gradient/Divergent Galerkin	$\mathcal{X}^{\alpha}_{ij}\mathbf{b_j}\delta_{\mathbf{ij}}\gamma^{\mathbf{T}}_\alpha$
	Mass SUPG	$\tau\mathcal{X}^{\alpha}_{ij}\mathbf{b}_j\bar{u}^h_i\gamma^T_\alpha$
	Advection SUPG	$\tau\left(\bar{\mathbf{u}}^h \otimes \bar{\mathbf{u}}^h\right)\mathcal{H}^{\alpha\beta}_{ii}\gamma_\alpha\gamma^T_\beta$
	Mass PSPG	$\tau\mathcal{X}^{\alpha}_{ij}\mathbf{b_j}\delta_{\mathbf{ij}}\gamma^{\mathbf{T}}_\alpha$
	Pressure Gradient PSPG	$\tau\mathbf{I}\mathcal{H}^{\alpha\beta}_{ii}\gamma_\alpha\gamma^T_\beta$
Temperature	Advective Galerkin	$\mathcal{X}^{\alpha}_{ij}\mathbf{b}_j\bar{u}^h_i\gamma^T_\alpha$
	Difusive Galerkin	$\mathbf{k}\mathcal{H}^{\alpha\beta}_{ii}\gamma_\alpha\gamma^T_\beta$
	Mass SUPG	$\tau_t\mathcal{X}^{\alpha}_{ij}\mathbf{b}_j\bar{u}^h_i\gamma^T_\alpha$
	Advection SUPG	$\tau_t\left(\bar{u}^h_i \otimes \bar{u}^h_i\right)\mathcal{H}^{\alpha\beta}_{ii}\gamma_\alpha\gamma^T_\beta$

Table 1: Stabilization terms summary.

As can be seen, the mass SUPG, and mass and pressure gradient PSPG matrices are also corrected. The first is equal to the advection Galerkin transpose multiplied by the SUPG/PSPG parameter. The second is equal to the divergent Galerkin also multiplied by the same parameter. The later is similar to the Galerkin viscous if the viscous tensor is taken as the identity matrix $\mathbf{I}_{3\times 3}$.

3 NUMERICAL RESULTS

3.1 Kim-Moin flow

The Kim-Moin problem is used to verify convergence rate of the solution of Navier-Stokes equations for both full and under integrated elements. The Kim-Moin flow has analytical solution for the incompressible viscous flow into a unity square. To emulate the 2D domain $\Omega = [0,1] \times [0,1]$, only one slice of hexahedra elements is used together with symmetric flow conditions for the perpendicular (z) direction.

This test problem was used by Föster et al. (2008) to investigate the influence of different stabilizations terms on the results obtained on distorted meshes. These numerical results were compared with the exact solution given by

$$u_x\left(x,y,t\right) = -\cos\left(a\pi x\right)\sin\left(a\pi y\right)e^{-2a^2\pi^2 t\nu}, \tag{35}$$

$$u_y\left(x,y,t\right) = \sin\left(a\pi x\right)\cos\left(a\pi y\right)e^{-2a^2\pi^2 t\nu}, \tag{36}$$

$$p\left(x,y,t\right) = -\frac{1}{4}\left(\cos\left(2a\pi x\right)+\sin\left(2a\pi y\right)\right)e^{-4a^2\pi^2 t\nu}. \tag{37}$$

The solutions of (35)-(37) are stationary in space and decrease monotonically in time. To keep the focus only in the spatial solution, the error is calculated scaling the temporal decay as shown bellow

$$\mathrm{err}_{\mathbf{u}} := \left\|\mathbf{u}^h - \mathbf{u}\right\|_2 e^{2a^2\pi^2 t\nu} \tag{38}$$

$$\mathrm{err}_{p} := \left\|p^h - p\right\|_2 e^{4a^2\pi^2 t\nu} \tag{39}$$

where the superscript h means the numerical solution.

The usual L^2 error norm employed in a-priori error estimates of each variable is replaced here by a root mean square norm (RMS) defined as follows,

$$\left\|\cdot\right\| := \left(\sum_{i=1}^{Nodes}\mathrm{err}_i^2\right)/Nodes \tag{40}$$

where the subscript i represents the error in each one of the nodes of the grid calculated with (38) and (39).

The computations are performed using undistorted and distorted grids which pattern is shown in Fig. 1. We adopt four different grid sizes: 44 × 44, 56 × 56, 68 × 68 and 80 × 80.

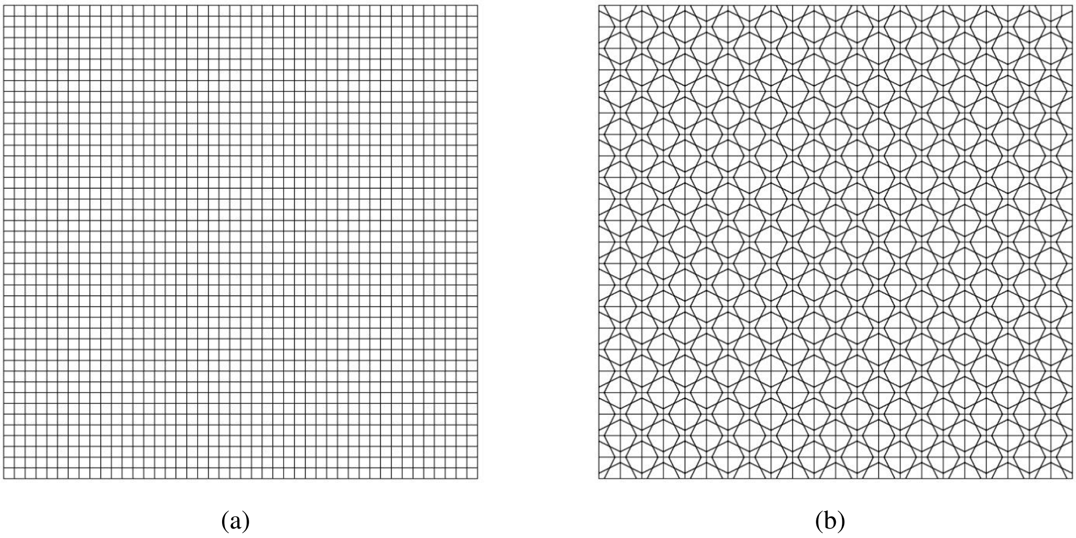
(a)

(b)

Figure 1: A sample of meshes for the error evaluation: (a) 44 × 44 undistorted mesh, (b) 44 × 44 distorted mesh

The results presented here were calculated using the parameter $a = 2$ and the kinematic viscosity $\nu = 0.01$. The time step for each grid size was calculated such as the maximum *CFL* number (based on the characteristic element size h^e) at $t = 0$ for the meshes is kept fix. This yields for the distorted meshes $CFL_d\,(0) = 0.2795$ and for the regular meshes $CFL_r\,(0) = 0.2530$. The Reynolds number was set to $Re = 100$ for all simulations. Finally, pressure is prescribed at the slice center such as $p\,(0.5, 0.5, z, t)$ is computed by (37).

The Table 2 and Table 3 show the RMS norms of the velocity, pressure and total (velocity plus pressure) errors for the four grids (distorted and undistorted meshes) calculated with full and under integrated elements. h^e_{av} means the average characteristic length of each mesh.

Mesh		Full			Reduced		
size	h^e_{av}	$\mathrm{err}_{\mathbf{u}}$	err_p	err_{u+p}	$\mathrm{err}_{\mathbf{u}}$	err_p	err_{u+p}
44×44	0.0282	0.00193	0.00808	0.00830	0.00310	0.00970	0.01019
56×56	0.0222	0.00133	0.00586	0.00600	0.00209	0.00693	0.00723
68×68	0.0182	0.00099	0.00453	0.00464	0.00152	0.00526	0.00547
80×80	0.0155	0.00079	0.00365	0.00373	0.00117	0.00418	0.00434

Table 2: Velocity and Pressure error for undistorted mesh.

Mesh		Full			Reduced		
size	h^e_{av}	$\mathrm{err}_{\mathbf{u}}$	err_p	err_{u+p}	$\mathrm{err}_{\mathbf{u}}$	err_p	err_{u+p}
44×44	0.0273	0.00268	0.00550	0.00612	0.00628	0,00778	0,00999
56×56	0.0218	0.00175	0.00432	0.00466	0.00405	0,00580	0.00707
68×68	0.0177	0.00127	0.00356	0.00376	0.00284	0,00458	0,00539
80×80	0.0150	0.00091	0.00302	0.00315	0.00210	0,00371	0,00426

Table 3: Velocity and Pressure error for distorted mesh.

As can be seen, the velocity filed always presents a smaller error than the calculated for the pressure. Comparing the results of the two mesh type patterns, we observe that, for the pressure variable, smaller errors were obtained on distorted meshes, resulting in smaller overall error too. Moreover the results with under-integration elements always present a higher error norm for each particular variable, which yields a higher overall error (velocity components plus pressure variables).

The spatial discretization error can be synthesized through an effective convergence rate defined from an error ansatz shown bellow (Eça and Hoekstra, 2009),

$$\mathrm{err}_i := \alpha_i h^{p_i}, \tag{41}$$

where p_i is the convergence rate error of each variable i.

The Fig. 2 shows the plot of $\log \mathrm{err}$ against $\log h_{av}$ comparing the results of full and under integrating for undistorted and distorted grids. The obtained rates are summarized in the Table 4.

Although smaller errors were obtained with full integration, higher convergence rates were found with under integration. The velocity variable always has a better convergence rate. The best result for velocity is achieved with one point integration and distorted mesh while for the

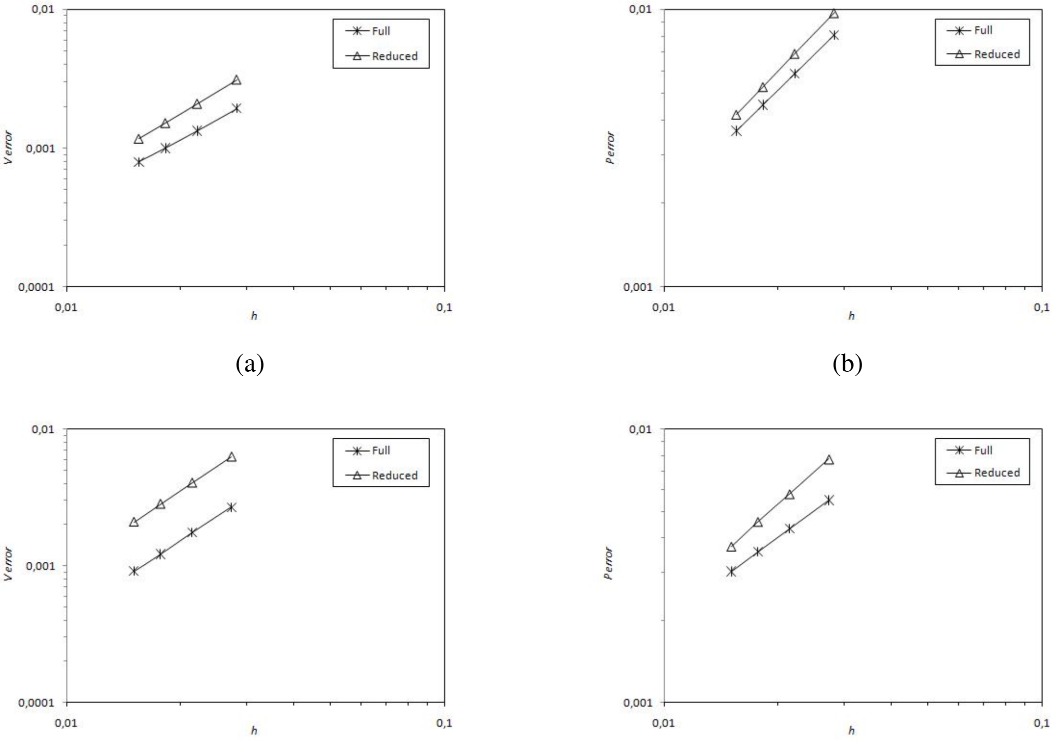

(a)

(b)

(c)

(d)

Figure 2: Spatial error discretization. Undistorted Meshes: (a) Velocity error, (b) Pressure error. Distorted Meshes: (c) Velocity error, (d) Pressure error

Mesh	Full			Reduced		
	$p_{\mathbf{u}}$	p_p	$p_{\mathbf{u}+p}$	$p_{\mathbf{u}}$	p_p	$p_{\mathbf{u}+p}$
Undistorted	1,49	1.32	1,33	1.63	1.41	1.43
Distorted	1.80	1.00	1.11	1.84	1.24	1.43

Table 4: Convergence rate.

pressure, it is also for the under-integrated element, but for the undistorted mesh. The worst result is obtained for the pressure with full integration and distorted mesh.

3.2 Three-dimensional natural convection with heated lateral walls

The second application example is the natural convection problem inside a unit cube. In this problem the right side wall $(x = 1)$ is kept cooler than the left one $(x = 0)$. The remaining walls are adiabatic. For the velocity, non-slip boundary conditions are imposed for the fluid at all walls. We prescribed the pressure at the center of the cavity as $p\,(0.5, 0.5, 0.5) = 0$.

The dimensionless physical parameters are given by the Reynolds number $Re = 11063$, the Prandtl number $Pr = 7$ and the Rayleigh number $Ra = 2.0 \times 10^5$. So the Grashof number is $Gr \approx 28571$. The thermal expansion coefficient is $\beta = 2.1 \times 10^{-4}$ and the gravity acceleration modulus is $|\vec{g}| = 1.1005$ aligned with the negative direction of the z axis. The cold temperature is $T_c = 0$ and the heat is $T_h = 1.0$ while the reference temperature is $T_\infty = T_c$. Further details about the physical parameters and how to rearrange them to yield dimensionless suitable quantities can be found in Griebel et al. (1997). There is an extensive literature on numerical results for this class of buoyancy force problem at many scales of the Rayleigh number. See Davis (1983) and Mayne et al. (2000) for instance.

The steady-state temperature field and the streamlines at the plane $y = 0.5$ are presented in Fig. 3. The Fig. 4 shows the spatial velocity vector field and the temperature over the $x = 1$, $y = 1$ and $z = 0$ planes.

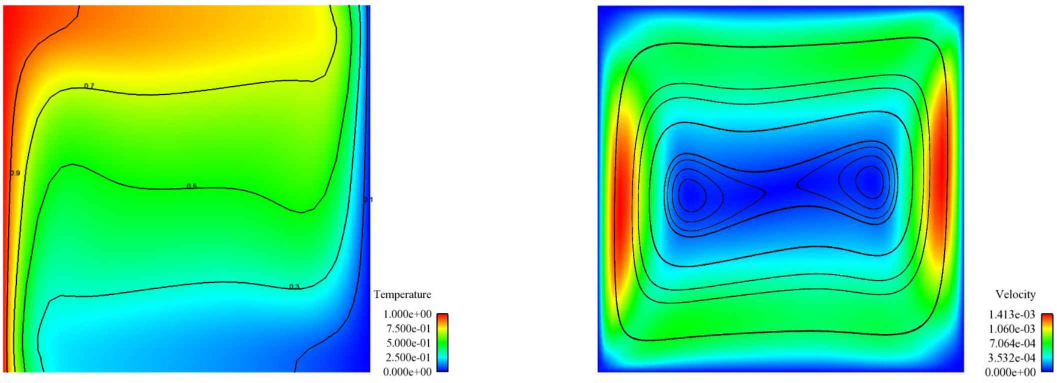

(a) (b)

Figure 3: Natural convection into a unit cube: (a) Temperature field and isotherms at $y = 0.5$, (b) Velocity field and streamlines over at $y = 0.5$

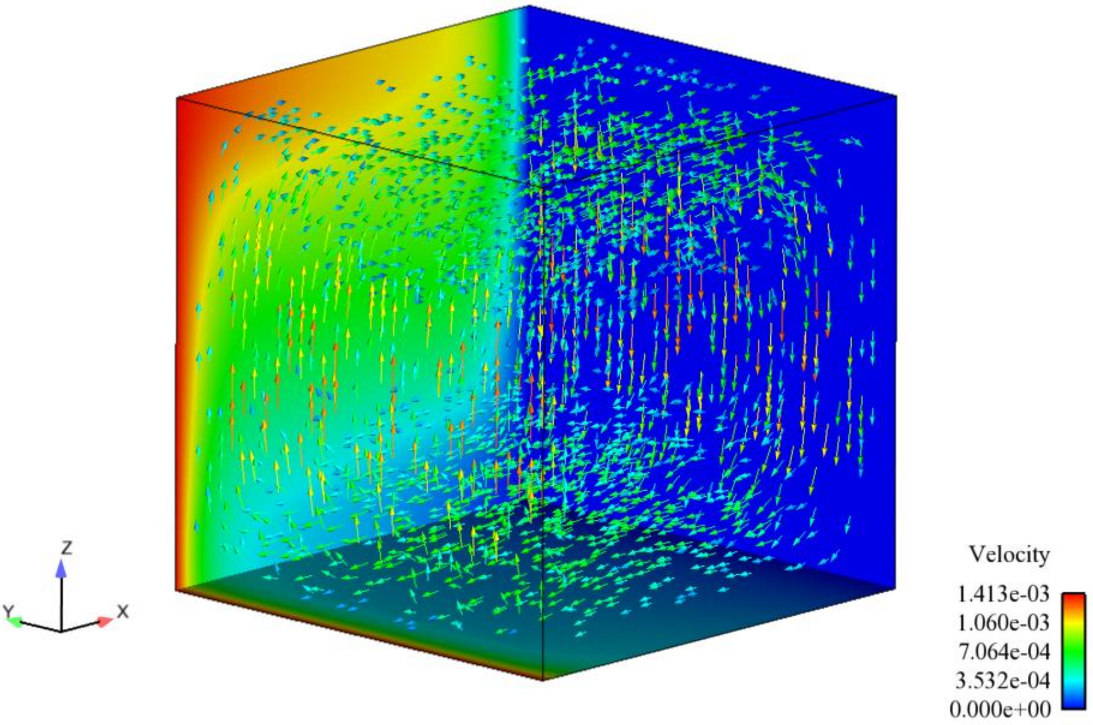

Figure 4: Spatial velocity vector field

Two different views of the spatial streamlines are presented in Fig. 5

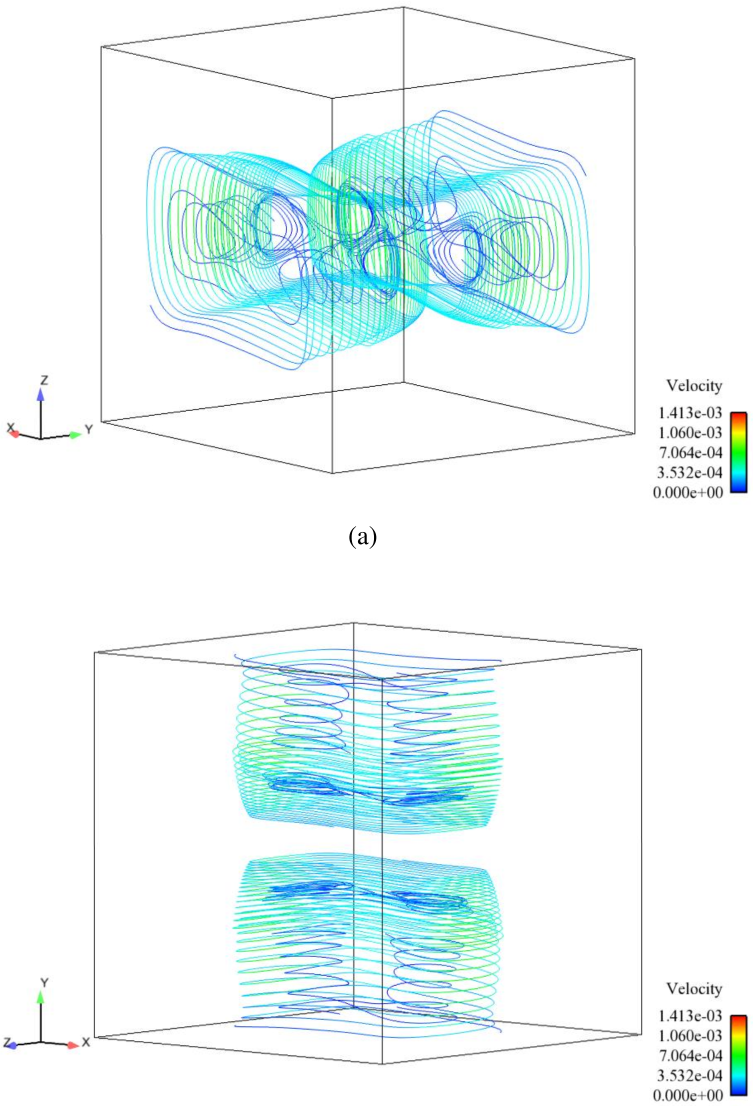

(a)

(b)

Figure 5: Natural convection into a unit cube: (a) First view, (b) Second view

The regular mesh has $32 \times 32 \times 32$ elements and the time step size is $\Delta t = 50$. In order to compare the performance of the full and under-integrated elements, we fixed the maximum time $t_{end} = 18000$.

The linear solver is the GMRES(30) and the linear tolerance was set 1×10^{-9} while the nonlinear tolerance was 1×10^{-4} for both Navier-Stokes and transport problems. PETSc provides parallel preconditioners that can be used with incomplete LU factorizations on each sub domain (on each processor). In the experiments we used a non-overlapping parallel incomplete factorization preconditioning (ILU(1)) together with Block-Jacobi.

This simulation was performed on the SGI Altix ICE 8200 cluster with 32 nodes. Each node has two Intel Xeon quad-core (2.66GHz / 4MB L2) and 8GB of memory. The nodes are connected by an InfiniBand network. The MPI over InfiniBand is Open MPI version 1.2.8.

We compare the parallel computational performance for the full and under-integration cases for the coupled viscous flow and temperature transport systems. The best results were obtained setting the hourglass stabilization parameters as $\epsilon_d = 1.0$, $\epsilon_a = 0.5$ and $\epsilon_p = 1.0$. The computed

CPU time in seconds are summarized in the following tables.

CPU	Navier-Stokes			Transport			Total
	Assembly	Solver	Total	Assembly	Solver	Total	
16	165.15	995.60	1160.75	41.93	111.75	153.68	1314.43
32	81.74	508.24	589.98	21.30	69.68	86.85	680.96
64	40.90	354.31	395.21	11.85	85.85	97,7	492.91

Table 5: CPU time in seconds to assemble and linear solver with full integration.

CPU	Navier-Stokes			Transport			Total
	Assembly	Solver	Total	Assembly	Solver	Total	
16	93.03	1043.63	1136.66	26.61	102.89	129.50	1266.16
32	46.28	501.07	547.35	14.11	55.94	70.05	617.40
64	24.85	357.25	382.10	9.65	83.60	93.25	475.35

Table 6: CPU time in seconds to assemble and linear solver with under-integration.

We observe that computing element matrices and assembling the Navier-Stokes and temperature transport systems and residuals is approximately two times faster for the under-integrated element. However, the time spent in the nonlinear solution procedure is roughly equivalent for both elements. Thus the overall CPU time of the under integration procedure does not present a significant gain over the full integration (5-10% faster). This is consistent with the behavior of the fully implicit time marching scheme employed here that uses preconditioned GMRES. The total number of the solver linear iterations (LI) and nonlinear iterations (NLI) are presented in the Table 7 and Table 8.

CPU	Navier-Stokes		Transport	
	LI	NLI	LI	NLI
16	1961	445	1152	532
32	2614	445	1789	536
64	2557	445	1933	549

Table 7: Linear and non-linear iteration summary for full integration.

CPU	Navier-Stokes		Transport	
	LI	NLI	LI	NLI
16	1834	445	1537	530
32	2664	442	2246	538
64	3081	442	2445	540

Table 8: Linear and non-linear iteration summary for under-integration.

As can be seen, the total number of linear and nonlinear iterations for the under-integrated element is equivalent to the full integrated element. This indicates that conditioning is not affected by the hourglass control. Further performance gains can be achieved by using solver strategies that compute residuals only, like Jacobian-Free Newton-Krylov methods (Knoll and Keyes, 2004).

4 CONCLUSIONS

We presented the results of a comparison of the solution of the Navier-Stokes and temperature transport using a stabilized finite element formulation for full and under-integrated hexaedron elements. The convergence rates obtained for both elements presented good agreement. A comparison of the parallel performance of full and under-integrated elements shows that the time spent in the nonlinear solution procedure is roughly equivalent for both elements. We have observed that computing element matrices, residuals and assembling the system matrix is twice as faster with elements with hourglass control than with the fully integrated elements. Better CPU performance for the under-integrated element is expected as the mesh size increases.

Acknowledgements

This work is partially supported by CNPq and ANP. We are also indebted to Engineering Simulation and Scientific Software (ESSS) to their partial support to A. Rossa in his PhD studies at COPPE/UFRJ.

REFERENCES

Belytschko T., Liu W., and Moran B. *Nonlinear Finite Element for Continua and Structures*. John Wiley & Sons, 2000.

Belytschko T., Ong W., and Kennedy J. Hourglass control in linear and nonlinear problems. *Computer Methods in Applied Mechanics and Engineering*, 43:251–276, 1984.

Christon M. A domain-decomposition message-passing approach to transient viscous incompressible flow using explicit time integration. *Computer Methods in Applied Mechanics and Engineering*, 148:329–352, 1998.

Davis G.D. Natural convection of air in a square cavity: A bench mark numerical solution. *International Journal for Numerical Methods in Fluids*, 3:249–264, 1983.

Dias C. and Coutinho A. Integração reduzida para problemas advectivos-difusivos escalares discretizados pela formulação SUPG com operador de captura de descontinuidades. *Revista Internacional de Métodos Numéricos para cálculo y Diseño en Ingeniería*, 14:145–166, 1997.

Dias C. and Coutinho A. Stabilized finite element methods with reduced integration techniques for miscible displacements in porous media. *International Journal for Numerical Methods in Engineering*, 59:475–492, 2004.

Eça L. and Hoekstra M. Evaluation of numerical error estimation based on grid refinement studies with the method of the manufactured solutions. *Computer & Fluids*, 38:1580–1591, 2009.

Föster C., Wall W., and Ramm E. Stabilized finite element formulation for incompressible flow on distorted meshes. *International Journal for Numerical Methods in Fluids*, 60:1103–1126, 2008.

Gresho P., Chan S., Lee R., and C.D. U. A modified finite element method for solving the time-dependent, incompressible navier-stokes equations, Part 1: Theory. *International Journal for*

Numerical Methods in Fluids, 4:557–598, 1984.

Griebel M., Dornseifer T., and Neuhoeffer T. *Numerical Simulation in Fluid Dynamics: A Practical Introduction*. SIAM, 1997.

Kirk B.S., Peterson J.W., Stone R., and Carey G.F. Libmesh: a c++ library for parallel adaptive mesh refinement/coarsing simulations. *Journal Engineering with Computers*, 22:237–254, 2006.

Knoll D. and Keyes D. Jacobian-free Newton-Krylov methods: a survey of approaches and applications. *Journal of Computational Physics*, 193:357–397, 2004.

Mallet M., Poirier C., and Shakib F. A new finite element formulation for computational fluid dynamics: Development of an hourglass control operator for multidimensional advective-diffusive systems. *Computer Methods in Applied Mechanics and Engineering*, 94:429–442, 1992.

Mayne D., Usmani A., and Crapper M. h-adaptive finite element solution of high rayleigh number thermally driven cavity problem. *International Journal of Numerical Methods for Heat and Fluid Flow*, 10:598–615, 2000.

Rossa A., Camata J., and Coutinho A. Stabilized SUPG/PSPG/LSIC FEM formulation using libMesh. *Proceedings of 30th CILAMCE,Armação dos Búzios, Rio de Janeiro/Brazil*, 2009.

Tezduyar T. Stabilized finite element formulations for incompressible flows computation. *Advances in Applied Mechanics*, 28:1–4, 1992.